3D LiDAR Aided GNSS NLOS Correction by Direction-of-Arrival Estimation Using Doppler Measurements in Urban Canyons

Xikun Liu, Weisong Wen*, *Member, IEEE*, Liyuan Zhang, Li-Ta Hsu, *Senior Member, IEEE*

***Abstract*—Global navigation satellite system (GNSS) positioning in urban environments suffers from significant accuracy degradation due to non-line-of-sight (NLOS) signal receptions. Existing correction methods, such as 3D model-aided and 3D LiDAR-aided GNSS, lack signal direction information and typically construct candidate reflection paths by exhaustively searching over possible reflection surfaces or azimuth angles, and selecting the final path based on the shortest-path assumption. However, this assumption is often invalid in dense urban canyons. To address this limitation, we propose a novel GNSS NLOS correction method that uses Doppler shift measurements to infer signal directional information, which is integrated with real-time point cloud mapping to reconstruct the actual signal reflection path actively. This approach allows us to directly track signal reflection, eliminating the need for exhaustive candidate generation and the shortest-path assumption. Experiments conducted on datasets collected in urban canyons demonstrate the effectiveness of the proposed method. Results show that the method achieves over 90% correction availability for NLOS signals, leading to more than 50% improvement in 3D GNSS positioning accuracy.**

***Index Terms*—3D LiDAR, Global navigation satellite system (GNSS), Perception-aided integration, NLOS correction, Doppler measurement model, Geometry distribution, Urban canyons**

I. Introduction

Positioning plays a fundamental role in intelligent transportation systems (ITS) [1]. Among various technologies, the Global Navigation Satellite System (GNSS) [2] is one of the most widely adopted solutions due to its capability to provide all-weather, global coverage positioning services [3]. In open sky conditions, commercial GNSS receivers can achieve sub-meter-level positioning accuracy with differential GNSS corrections from the reference station. However, achieving accurate GNSS positioning in urban areas remains a challenge [4, 5]. This is primarily due to signal interference caused by surrounding structures, particularly high-rise buildings that block or reflect GNSS signals. This interference includes two types: The first is non-line-of-sight (NLOS), where the signal reaches the receiver after reflection. The second is multipath, where several reflected signals from a satellite are received (with or without a line-of-sight (LOS) signal) [6]. The new L5 frequency can help reduce multipath effects [7]. In contrast, NLOS is often hard to mitigate and typically causes larger observation errors. For example, as shown in Fig. 1, the NLOS signal from satellite G4 caused a pseudorange error of over 100 meters. These NLOS errors reduce the reliability of GNSS and limit its use in ITS applications in urban environments.

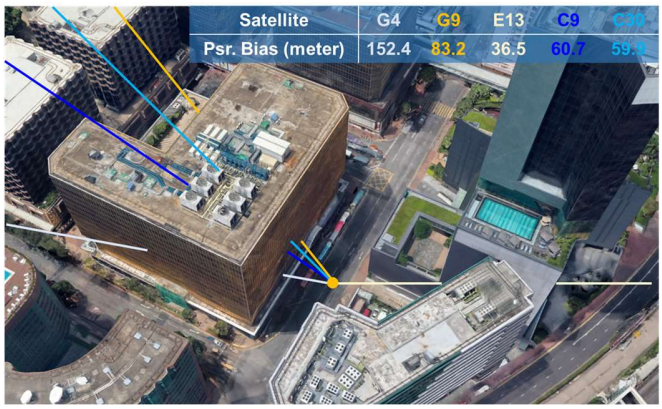

Fig. 1. Demonstration of satellite signal receptions in an urban canyon of Hong Kong. The receiver position is marked as a yellow dot. The colored lines are Line-of-Sight (LOS) transmission paths of satellite signals. A list of the pseudorange observation error (denoted as Psr. Bias in the figure) is given in the table in the upper right corner.

To address the challenges posed by NLOS reception in urban

This work was supported in part by the Innovation and Technology Fund under the project "Safety-Certified Multi-Source Fusion Positioning for Autonomous Vehicles in Complex Scenarios (ZPE8)", in part by the Germany/Hong Kong Joint Research Scheme under the project "Maximum Consensus Integration of GNSS and LiDAR (RADM)", and in part by the Research Center of Deep Space Exploration (RC-DSE) under the project "Multi-Robot Collaborative Operations (BBDW)". This paper is also funded by the PolyU Research Institute for Advanced Manufacturing (RIAM) under the project “Unmanned Aerial Vehicle Aided High Accuracy Addictive Manufacturing for Carbon Fiber Reinforced Thermoplastic Composites Material (CD8S)”.

Xikun Liu, Weisong Wen, Liyuan Zhang, and Li-Ta Hsu are all with Hong Kong Polytechnic University, Hong Kong (correspondence e-mail: welson.wen@polyu.edu.hk).

GNSS positioning, several strategies have been proposed. One common approach is fault detection and exclusion (FDE) [8, 9], which attempts to identify and remove faulty NLOS measurements using consistency check. However, in dense urban environments where multiple fault signals dominate, FDE may fail to isolate faulty measurements. Moreover, excluding NLOS signals reduces the number of available satellites, which further affects satellite geometry and degrades positioning accuracy. Another approach involves 3D model-aided (3DMA) GNSS methods [10, 11], which use building models and ray-tracing techniques to predict potential reflection paths and correct NLOS measurements. More recently, with advances in perception and mapping technologies, 3D LiDAR-aided (3DLA) methods have been developed using real-time point cloud map (PCM) without relying on prior building models [12, 13]. These methods perform exhaustive searches over candidate reflection points in the point cloud to recover the signal path. Despite their differences, both 3DMA and 3DLA methods share a common limitation: the final reflection path is selected from candidate paths based on the shortest-path assumption. Due to the lack of physical surface information, these methods assume that signals with the shortest reflection paths are most likely to be received. However, this assumption often fails in urban areas, where long-range reflections from highly reflective surfaces (e.g., glass curtain walls) can dominate the received signals. Therefore, it is necessary to explore a new method that can achieve reliable NLOS correction and does not rely on the shortest-path assumption.

In this work, we focus on GNSS Doppler observations, which describe the relative motion between the receiver and the signal source and implicitly contain information about the signal's direction of arrival (DOA). In NLOS conditions, the signal source becomes the reflection point. By analyzing Doppler measurements along with prior knowledge of receiver motion, we can estimate the DOA of the reflected signal. Combined with the 3D environment reconstructed by LiDAR, this directional cue enables us to directly trace back to the signal's reflection point and recover the true NLOS signal path. To effectively and reliably perform GNSS NLOS correction in actual systems, this paper proposes a 3D LiDAR-aided GNSS NLOS correction method based on DOA estimation using Doppler measurements. The contributions of this work can be concluded as follows:

(1) This paper proposes a 3D LiDAR-aided GNSS signal DOA estimation method using the Doppler measurement, together with a thorough accuracy analysis of DOA estimation based on LiDAR-derived prior velocity.
(2) This paper proposes a 3D LiDAR-aided GNSS NLOS correction framework leveraging signal DOA and LiDAR PCM, with further consideration on signal penetration, mapping inaccuracies, and DOA estimation error.

To the best of our knowledge, this work represents the first attempt to accurately track NLOS signal paths for urban GNSS applications by integrating 3D LiDAR and GNSS Doppler measurements. The rest of this paper is organized as follows: Section II discusses the relevant work. Section III defines the notations and provides an overview of the proposed framework. Section IV details the methodology, including the 3DLA GNSS DOA estimation and the NLOS correction pipeline. Section V presents experimental results and evaluations of the proposed method. Finally, Section VI concludes the paper and outlines potential directions for future research.

II. Related Work

A. FDE mitigates faulty measurements but deteriorates the satellite geometry by reducing satellite number.

FDE [8, 9] improves GNSS positioning by identifying and removing faulty measurements. The core idea is to detect inconsistencies among redundant satellite measurements or between predicted and actual observations. However, traditional FDE tends to degrade in urban areas where signal distortions are more prevalent and harder to model accurately. Researchers have also used cameras [14, 15] or Light Detection and Ranging (LiDAR) sensors [16, 17] to capture environment and predict satellite visibility for NLOS exclusion. However, tall buildings in urban areas often cause severe signal blockage, resulting in limited sky visibility and fewer visible satellites. This poor satellite geometry can significantly degrade positioning accuracy and increase estimation uncertainty. Although excluding NLOS signals can improve observation quality, it further affects the already limited satellite geometry. Therefore, correcting rather than excluding NLOS signals is critical for urban GNSS positioning.

B. 3DMA GNSS Tracks Signal Reflections with Limitations in Modeling and Assumptions.

In recent years, researchers have developed 3DMA GNSS to correct NLOS errors using ray-tracing techniques [10, 11, 18-20]. The 3DMA GNSS determines signal paths within a 3D building map by the following three steps [18]: (1) Find where the signal intersects with building surfaces, (2) Build the signal path and compute the total travel distance, (3) Choose the shortest path as the final signal route. This shortest-path assumption is made because the material properties of building surfaces are often unknown. It assumes that the shortest path keeps the strongest signal, increasing the chance of reception [18]. The predicted signal path is used to correct NLOS errors. This is done by subtracting the extra travel distance compared to the LOS path. However, the 3DMA GNSS method has several limitations. First, it requires comprehensive, city-scale 3D building models, which makes it ineffective for unmodeled objects, e.g., dynamic vehicles. Second, its performance is limited by large initial position errors, which are common in urban environments. Third, its NLOS correction becomes unreliable when the reflection path is long due to the reliance on the shortest path assumption. These limitations reduce the reliability and real-world usability of 3DMA GNSS methods in urban environments.

C. 3DLA GNSS Addresses Model Challenges, but the Shortest Path Assumption Persists.

To address the model requirement by 3DMA, the 3DLA GNSS methods have been developed. Unlike 3D building models, LiDAR provides real-time 3D point clouds that capture the detailed geometry of surrounding buildings and moving objects. Moreover, the PCM is reconstructed in a sensor-centric manner, which avoids the initialization issues of 3DMA GNSS. Recent advancements have integrated single-frame LiDAR scans with public building height data to detect and correct NLOS signals [12, 21]. Building surfaces are extracted through segmentation, and their boundaries are extended using height information. NLOS signals are then modeled based on azimuth angle, elevation angle, and distance to the building surface. However, segmentation becomes unreliable when building surfaces are irregular or occluded. To improve the field of view (FOV) of LiDAR and avoid using building height data, some approaches combine LiDAR with a sky-facing camera for NLOS detection [22]. To essentially address the FOV limitation and support reflection detection on complex facades, LiDAR Simultaneous Localization And Mapping (SLAM) is introduced in 3DLA methods with PCM-based reflection point searching [13]. To be more specific, point clouds from adjacent frames are merged to reconstruct a PCM. The system uses the PCM, receiver position, and LOS vector to detect occlusion and predict NLOS receptions. Then, the system searches across azimuth angles at a fixed elevation to find candidate reflection points. The final reflection point and path are chosen based on the shortest-path assumption, as in 3DMA GNSS. However, this assumption oversimplifies real signal propagation and reduces the accuracy of 3DLA-based NLOS correction.

D. DOA Estimation using Doppler Measurement.

Traditional GNSS DOA estimation uses antenna arrays to measure phase or time differences of incoming signals [23], but such systems are impractical for most urban ITS applications. In addition to pseudorange and carrier phase, there are Doppler measurements, which can be used to estimate receiver velocity [24, 25]. The Doppler effect reflects frequency shifts due to relative motion between the receiver and the signal source. In LOS condition, the Doppler shift reflects the relative motion between the satellite and the receiver. In contrast, under NLOS conditions, the signal reflects off a surface before reaching the receiver. In such cases, the Doppler frequency reflects the relative motion between the reflection point and the receiver [26]. Therefore, the Doppler shift under NLOS inherently encodes the DOA from the reflection point to the receiver. Yet, estimating DOA from Doppler measurements remains difficult in practice. Only a few studies have explored using single-antenna Doppler data for DOA estimation. Recently, [25] showed that DOA can be estimated from Doppler using ground-truth velocity, and validated it with ray-tracing simulations. For real-world applications, obtaining reliable receiver velocity remains an obstacle. Fortunately, such velocity can be estimated from LiDAR-derived motion estimation. The method in [25] also relies on exhaustive angular searches to estimate DOA. This creates a computational load, especially when processing signals from multiple satellites. Moreover, it is difficult to balance resolution, accuracy, and efficiency when choosing DOA sampling intervals.

TABLE I
NOTATIONS

Notation	Description	Notation	Description
t	GNSS epoch	$\dot{\delta}$	Clock bias drift
s	Satellite index	c	Speed of light
w	Master satellite index	res	Residual
r	Receiver	$rang$	Range
e	Reference station	$\mathbf{e}$	Unit vector
λ	Wavelength	$\mathbf{v}$	Velocity
d	Doppler measurement	$\mathbf{p}$	Position
ρ	Pseudorange measurement	$\boldsymbol{l}$	Transmission vector

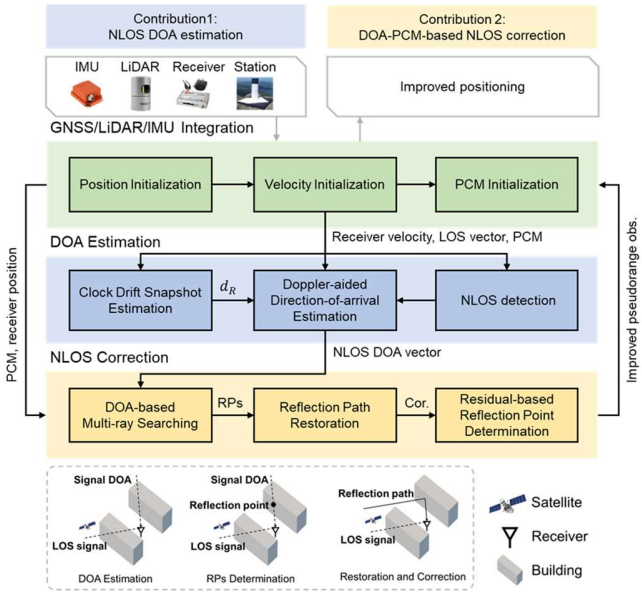

Fig. 2. The overview of the system pipeline.

III. NOTATIONS AND SYSTEM OVERVIEW

A. Notations

Uppercase bold letters represent matrices, and lowercase bold letters represent vectors. Italic letters denote variables and frame coordinates. Plain lowercase letters represent constant scalars. Table I lists the major notations used in the following sections.

B. System Overview

The proposed method, shown in Fig. 2, consists of three main stages. First, the system is initialized using GNSS/LiDAR/IMU integrated odometry to estimate the initial position, velocity,

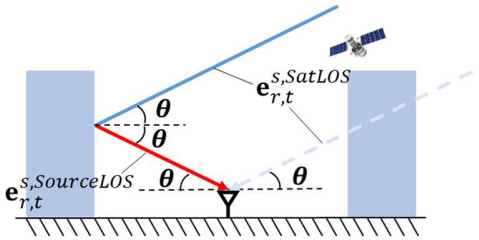

Fig. 3. Demonstration of directional vector for NLOS reception. The blue boxes are buildings, the blue line and dash line represent the LOS transmission direction, the red line represents the NLOS reflection transmission direction,θ represents the elevation angle.

and PCM. In this stage, we use an open-source, tightly-coupled GNSS/LiDAR/IMU odometry system (GLIO) [27]. In the second stage, the receiver's clock bias drift is estimated in snapshot mode, together with GNSS signal DOA estimation. The third stage includes restoring candidate reflection paths, evaluating pseudorange corrections, and final positioning based on the corrected observations. For simplicity, all states and positions are represented in an Earth-Centered, Earth-Fixed (ECEF) frame throughout this paper.

IV. Methodology

A. 3D LiDAR aided GNSS Signal Direction-of-Arrival Estimation using Doppler Measurement

This section presents the 3D LiDAR-aided DOA estimation method based on Doppler observations. It covers the first two stages introduced in the system overview. The discussion includes the Doppler observation model for NLOS signals, the system initialization process, and the optimization-based DOA estimation using Doppler data. The first part provides the theoretical background, and the other two focus on the implementation details of the proposed method.

Doppler Observation Modeling for NLOS Signal

This subsection analyzes the influence of signal reflection on Doppler measurements. The corresponding observation model is defined as [26]:

$$\lambda d_{r,t}^{s} = \mathbf{e}_{r,t}^{s,SatLOS}\mathbf{v}_{s,t} - \mathbf{e}_{r,t}^{s,SourceLOS}\mathbf{v}_{r,t} + \mathrm{c}\left(\dot{\delta}_{r,t} - \dot{\delta}_{s,t}\right) + \varsigma_{r,t}^{s} \quad (1)$$

where λ represents the signal wavelength for each satellite, $d_{r,t}^{s}$ is the Doppler measurement from the receiver. The satellite and receiver velocities are given by $\mathbf{v}_{s,t}$ and $\mathbf{v}_{r,t}$, respectively. $\varsigma_{r,t}^{s}$ denotes the Doppler observation noise. $\mathrm{c}\left(\dot{\delta}_{r,t} - \dot{\delta}_{s,t}\right)$ represents the clock drift-induced observation bias, where c is the speed of light. The satellite clock bias drift $\dot{\delta}_{s,t}$ can be calibrated in advance, while the receiver clock drift $\dot{\delta}_{r,t}^{i}$ is unknown and needs to be estimated. $\mathbf{e}_{r,t}^{s,SatLOS}$ denotes the unit vector from the receiver to the satellite. $\mathbf{e}_{r,t}^{s,SourceLOS}$ denotes the LOS vector from the receiver to the signal source, which corresponds to signal DOA. Under LOS conditions, $\mathbf{e}_{r,t}^{s,SourceLOS}$ is equal to $\mathbf{e}_{r,t}^{s,SatLOS}$. However, in NLOS receptions, as illustrated in Fig. 3, the receiver receives only the reflected signal. In this case, $\mathbf{e}_{r,t}^{s,SourceLOS}$ represents the LOS vector between the receiver and the reflection point, not the satellite. Given the receiver velocity and clock drift, the Doppler measurement provides the angle between the receiver velocity and $\mathbf{e}_{r,t}^{s,SourceLOS}$, as shown in (1). This relationship serves as a constraint for estimating the DOA. Furthermore, assuming most reflecting planes are vertical, the elevation angle θ of the reflected signal equals to that of the LOS path. This provides an additional constraint for DOA estimation. Together, these constraints form the theoretical basis for estimating the signal DOA ($\mathbf{e}_{r,t}^{s,SourceLOS}$).

System Initialization and Receiver Clock Bias Drift Estimation

Based on the Doppler observation model, initializing both the receiver velocity and clock bias drift is required for DOA estimation. We use GLIO [27], a tightly coupled integration system for velocity initialization. It fuses differential GNSS [28], LiDAR, and IMU measurements. The factor graph design in GLIO ensures global consistency between GNSS and LiDAR measurements, enabling reliable velocity estimation even in highly urbanized areas.

After velocity initialization, we estimate the receivers' clock bias drift in snapshot mode using Doppler observations from all satellites at a given epoch. Under the assumption of pure LOS reception, the receiver clock bias drift can be calculated from a single Doppler observation according to (1):

$$\dot{\delta}_{r,t} = \left(\lambda d_{r,t}^{s} - \mathbf{e}_{r,t}^{s,SatLOS}\mathbf{v}_{s,t} + \mathbf{e}_{r,t}^{s,SatLOS}\mathbf{v}_{r,t} + \dot{\delta}_{s,t}\right)/\mathrm{c} \quad (2)$$

By averaging Doppler observations over all visible satellites, random measurement noise is reduced, which enables reliable estimation of the receiver's clock bias drift [25].

Optimization-based DOA Estimation

Estimating the signal DOA essentially requires determining a two-degree-of-freedom (DoF) rotation: the elevation angle and the azimuth angle. The elevation angle is determined under the assumption that the reflected signal shares the same elevation as the LOS signal. As a result, DOA estimation is simplified to a one DoF problem that estimates the azimuth angle given a fixed elevation. In this paper, we reformulate the problem as estimating a rotation angle α of the LOS vector about the vertical axis. This rotation inherently satisfies the elevation angle constraint. The observation equation for this rotation angle can be derived from the Doppler observation equation. Specifically, we take the ground normal vector $\hat{\mathbf{p}}_{r,t}$ as the vertical axis, which is calculated by normalizing the receiver's ECEF coordinate $\mathbf{p}_{r,t}$. Then the DOA vector $\mathbf{e}_{r,t}^{s,SourceLOS}$ is then modeled as a rotation of the LOS vector $\mathbf{e}_{r,t}^{s,SatLOS}$ around the ground normal vector $\hat{\mathbf{p}}_{r,t}$ by the angle α. Mathematically, $\mathbf{e}_{r,t}^{s,SourceLOS}$ is given by:

$$\begin{aligned}\mathbf{e}_{r,t}^{s,SourceLOS} = {} & \cos\alpha\,\mathbf{e}_{r,t}^{s,SatLOS} \\ & + (1-\cos\alpha)\left(\hat{\mathbf{p}}_{r,t}\cdot\mathbf{e}_{r,t}^{s,SatLOS}\right)\hat{\mathbf{p}}_{r,t} \\ & + \sin\alpha\left(\hat{\mathbf{p}}_{r,t}\times\mathbf{e}_{r,t}^{s,SatLOS}\right)\end{aligned} \quad (3)$$

Given the initialized velocity and estimated receiver clock bias drift, a Doppler observation function with respect to α can be constructed by combining (1) and (3). Based on this model, the

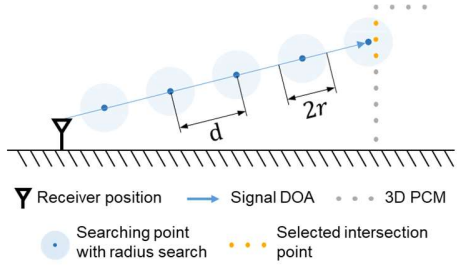

Fig. 4. Demonstration of intersection point searching.

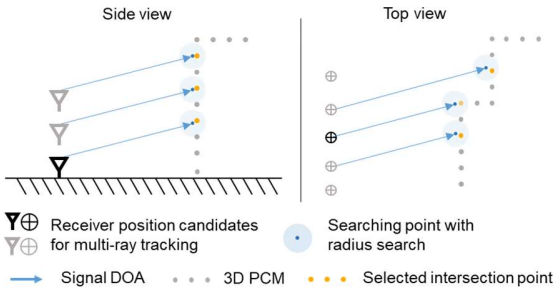

Fig. 5. Demonstration of multi-ray tracking with given receiver position and signal DOA.

Doppler constraint for estimating α can be formulated through a residual defined as:

$$res_{r,t}^{s,DoppDOA} = \lambda d_{r,t}^{s} - \lambda d_{r,t}^{s,predict} \tag{4}$$

where $d_{r,t}^{s,predict}$ is the predicted Doppler measurement for a given α. Accordingly, the DOA estimation for all satellites at epoch t can be formulated as the following optimization problem:

$$\chi^{*} = \underset{\chi}{\operatorname{argmin}} \sum_{S} \left(\left\| res_{r,t}^{s,DoppDOA} \right\|^{2} \right) \tag{5}$$

where the state variable is defined as:

$$\chi = [a_r^0, \cdots, a_r^s] \tag{6}$$

For each satellite s, we optimize α to minimize the Doppler residual $res_{r,t}^{s,DoppDOA}$ and obtain the estimated DOA based on (3). It is worth noting that the right-hand side of (3) can be expressed as a combination of $\cos\alpha$ and $\sin\alpha$ with different coefficients. This expression can be simplified into a single cosine function, which means the optimization involves solving a cosine equation, which yields two possible solutions for α. The final DOA is selected and validated jointly with the subsequent NLOS correction process.

B. DOA-based NLOS Correction with 3D PCM

This section introduces the restoration of reflection paths based on DOA estimation, followed by NLOS correction. We assume a single reflection for each NLOS signal. To identify potential NLOS signals, we perform detection by combining our previous 3DLA NLOS detection method [22] with a residual check based on the initialized receiver positions. Satellites that are occluded in the PCM and have double-difference (DD) pseudorange residuals exceeding a predefined threshold are classified as NLOS. In our implementation, the threshold is experimentally set to 5 meters. Note that some multipath signals may also be classified as NLOS in this approach.

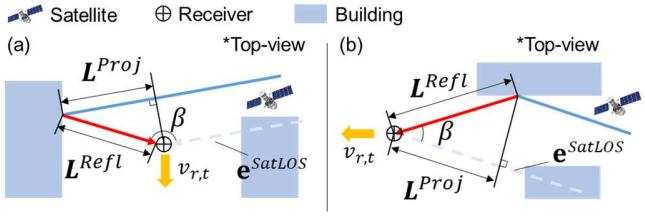

Fig. 6. Two cases of NLOS correction.

Intersection point searching for Reflection Point Determination

The reflection point is determined by finding the intersection between the DOA ray from the receiver and the 3D PCM. The search strategy was originally developed in our previous 3DLA NLOS detection and correction methods [13]. It performs a nearest-point search using a sliding search sphere, as depicted in Fig. 4. The search begins with the receiver's position as the initial center. The search center slides along the DOA direction with a step size of d. At each search region, a nearest neighbor search is performed within the 3D PCM using a radius r. Initially, the search space does not intersect with any surface, therefore, no points are returned. Once a point is found within the search radius, it is considered a potential reflection point. The search process then terminates. The maximum searching range is 100 meters. The values of step size d and radius r depend on the resolution of 3D PCM. First, the search radius r must be larger than PCM resolution to avoid missing intersections (e.g., "tunneling" through objects). Second, we deliberately set r and step size d such that neighboring search regions overlap, ensuring small structures are not missed during the search. In our implementation, d is set to 0.5 meters and r to 0.8 meters.

Multi-Ray Tracking

The accuracy of NLOS DOA estimation may be affected by errors in the initial velocity, Doppler measurement noise, or receiver clock drift. These factors can further impact the determination of the reflection point. More importantly, environmental factors such as vegetation, dynamic objects, and smooth surfaces (e.g., glass curtain walls) can degrade the reliability of reflection point determination. Since reflection point identification relies on occlusion detection, sparse vegetation makes it difficult to distinguish between reflected and penetrated signals. Meanwhile, point clouds containing dynamic objects or smooth surfaces often fail to represent the true reflective environment. To address these challenges, we propose a multi-ray searching strategy inspired by conventional 3DMA GNSS candidate sampling, as illustrated in Fig. 5. This method leverages the structural similarity of nearby environments within a small region. Based on the antenna position and the signal DOA, we generate multiple candidate antenna positions. For each candidate, we search for intersection points to obtain possible reflection points and signal paths. Antenna sampling is conducted in two directions: along the vehicle's driving direction and along the vertical axis. This choice ensures that changing the antenna position does not

alter its relative distance to the buildings. Since the street direction is not explicitly estimated, the vehicle's driving direction is used as an approximation. To balance computational cost and accuracy, the sampling range is set to ±7 meters in the driving direction and 0-3 meters in the vertical direction. Additionally, the sampling resolution is set to 1 meter. This strategy expands the reflection search space by leveraging environmental similarity within a local region, without significantly altering the signal DOA. For each NLOS reception, the reflection point search is performed twice to account for the two DOA solutions.

NLOS Correction Formulation and Validation

For each NLOS reception, two sets of reflection point candidates are generated based on two DOA solutions. Each candidate's reflection path is reconstructed by connecting the receiver position, the reflection point, and the satellite in sequence. NLOS correction is then performed by calculating the additional travel distance of the reflected signal, which is the difference between the direct LOS path and the reflection path. Two models are used based on the angle β between the reflected and LOS signal, which is shown in Fig. 6. When β is larger than 90 degrees, the correction term for the pseudorange observation is calculated by:

$$\nabla\rho = \left\|\boldsymbol{L}^{Refl}\right\| + \left\|\boldsymbol{L}^{Proj}\right\| \tag{7}$$

$$\left\|\boldsymbol{L}^{Proj}\right\| = \left\|\boldsymbol{L}^{Refl} * \mathbf{e}^{SatLOS}\right\| = -\left\|\boldsymbol{L}^{Refl}\right\| cos\,\beta \tag{8}$$

where $\boldsymbol{L}^{Refl}$ is the vector from the receiver to the reflection point, $\boldsymbol{L}^{Proj}$ is the projection of $\boldsymbol{L}^{Refl}$ onto the LOS vector $\mathbf{e}^{SatLOS}$. $\|\cdot\|$ represents vector norm.

When β is smaller than 90 degrees, the correction term is calculated by:

$$\nabla\rho = \left\|\boldsymbol{L}^{Refl}\right\| - \left\|\boldsymbol{L}^{Proj}\right\| \tag{9}$$

$$\left\|\boldsymbol{L}^{Proj}\right\| = \left\|\boldsymbol{L}^{Refl} * \mathbf{e}^{SatLOS}\right\| = \left\|\boldsymbol{L}^{Refl}\right\| cos\,\beta \tag{10}$$

Combining (7) to (10), the correction formulation is summarized as:

$$\nabla\rho = \left\|\boldsymbol{L}^{Refl}\right\| * (1 - \cos\beta),\ \beta \in (0,\ \pi) \tag{11}$$

The final reflection point for each NLOS reception is selected by applying a residual check to validate all candidates. In this work, we perform residual check based on DD pseudorange residuals:

$$\rho^{s}_{DD,r,t} = \left(\rho^{s}_{r,t} - \rho^{s}_{e,t}\right) - \left(\rho^{w}_{r,t} - \rho^{w}_{e,t}\right) \tag{12}$$

$$\mathrm{r}^{s}_{DD,\rho,r,t} = \rho^{s}_{DD,r,t} - \left(rang^{s}_{r,t} - rang^{s}_{e,t}\right) - \left(rang^{w}_{r,t} - rang^{w}_{e,t}\right) \tag{13}$$

where the range distances $rang^{s}_{r,t}$, $rang^{s}_{e,t}$, $rang^{w}_{r,t}$ and $rang^{w}_{e,t}$ are calculated based on the initialized receiver position $\mathbf{p}_{r,t}$:

$$rang^{s}_{r,t} = \left\|\mathbf{p}_{r,t} - \mathbf{p}_{s,t}\right\|, rang^{s}_{e,t} = \left\|\mathbf{p}_{e} - \mathbf{p}_{s,t}\right\|,$$
$$rang^{w}_{r,t} = \left\|\mathbf{p}_{r,t} - \mathbf{p}_{w,t}\right\|, rang^{w}_{e,t} = \left\|\mathbf{p}_{e} - \mathbf{p}_{w,t}\right\| \tag{14}$$

where $\mathbf{p}_{s,t}$ and $\mathbf{p}_{w,t}$ are satellite positions, $\mathbf{p}_{e}$ is the position of the reference station. The final correction candidate is selected by minimizing the difference between $\mathrm{r}^{s}_{DD,\rho,r,t}$ and $\nabla\rho$.

V. Experimental Evaluation

The proposed method is evaluated on two challenging sequences from the open-source *UrbanNav* dataset, collected in Hong Kong [29]. Fig. 7 shows the experimental trajectories and environment, which feature densely packed buildings and tall trees. Such an environment leads to significant GNSS NLOS and multipath effects. In the following sections, we evaluate the proposed method in four aspects: (1) the impact of velocity bias on DOA estimation, (2) the accuracy of NLOS correction, (3) positioning performance with and without the proposed NLOS correction, and (4) computational efficiency. Notably, only driving periods are evaluated. The proposed method is implemented in post-processing using C++ and ROS [30], and the optimization is performed via Ceres Solver [31].

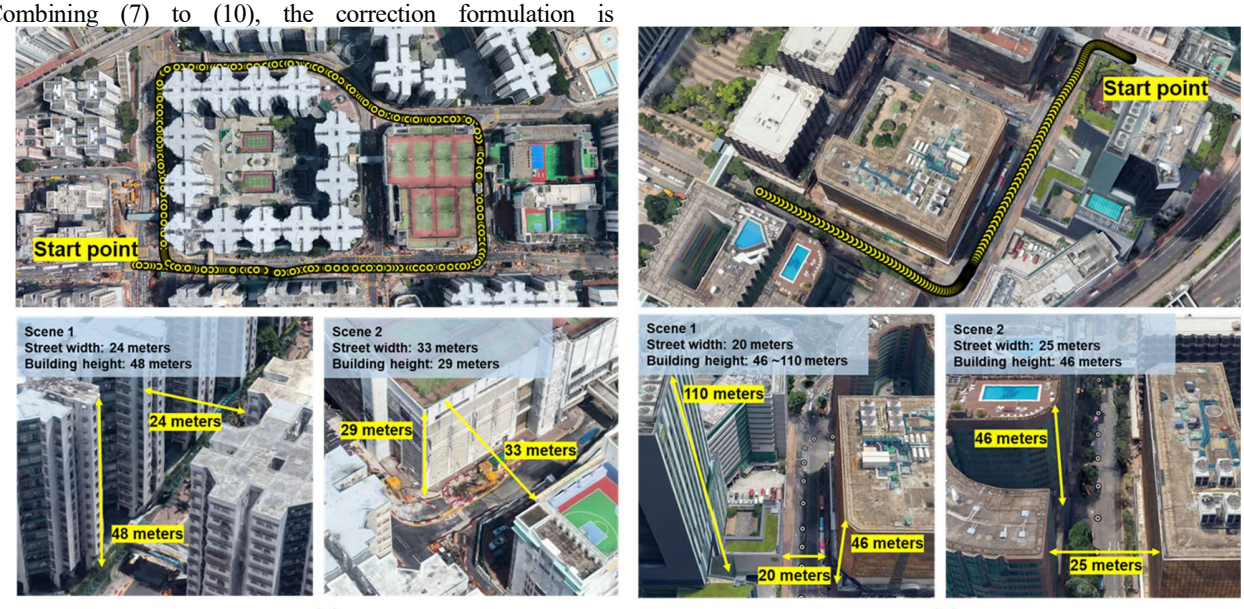

Fig. 7. The trajectory of the vehicle in the evaluation, together with demonstrations of data collection scenes.

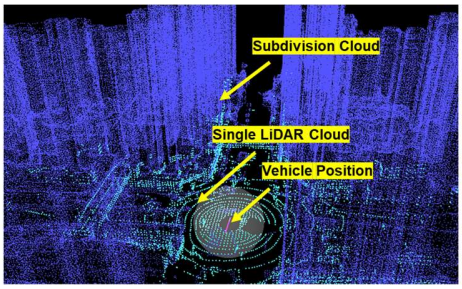

Fig. 8. The demonstration of a point cloud segment from public dataset and a single LiDAR scan.

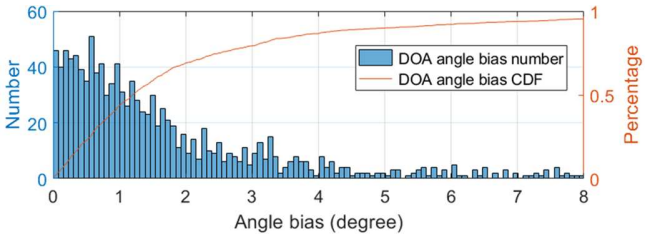

Fig. 9. The distribution and the cumulative distribution function (CDF) of the angle bias between the estimated DOA and the satellite LOS in the open-sky area.

A. Experiment Setup

The data collection platform is described in the *UrbanNav* dataset [29]. It includes a u-blox F9P GNSS receiver for raw single-frequency GPS/BeiDou signals at 1 Hz, an Xsens Ti-10 IMU for inertial measurements at 100 Hz, and a Velodyne HDL-32E LiDAR for point cloud scans at 10 Hz. Ground truth is provided by the NovAtel SPAN-CPT system, which integrates a high-precision multi-frequency, multi-constellation GNSS receiver with a tactical-grade inertial sensor to ensure absolute accuracy. All data sources are well-synchronized, with calibrated time alignment and extrinsic parameters. To address the limited FOV of a single LiDAR during the evaluation, we enhance the point cloud data using a public 3D city dataset in Hong Kong [32]. The large-scale PCM is divided into 100 × 100 meter local segments, each with a resolution of 1 meter. At each epoch, the corresponding segment is transformed based on the initialized position from GLIO, simulating a local 3D point cloud map, as shown in Fig. 8.

B. Evaluation of Velocity Bias on DOA Estimation

To assess the accuracy of the proposed DOA estimation method, we use satellite observations collected in suburban areas, where signals are assumed to closely follow the LOS direction. The DOA is estimated using Doppler measurements and the ground-truth vehicle velocity. The estimated DOA is then compared to the original LOS direction. Fig. 9 presents the distribution of the angular difference between the estimated DOA and the LOS direction, referred to as the DOA angle bias. The results indicate that, for most satellites, the estimated DOA aligns closely with the LOS direction, despite the presence of observation noise. Specifically, the Cumulative Distribution Function (CDF) shows that over 80% of the cases have deviations within 4 degrees. A small number of satellites exhibit larger discrepancies , likely caused by environmental interference.

TABLE II
SATELLITE INFORMATION (PRN: PSEUDORANDOM NOISE CODE, ELE.: ELEVATION ANGLE, IA: INCLUDED ANGLE BETWEEN THE DIRECTION OF RECEIVER VELOCITY AND SATELLITE LOS VECTOR)

PRN	17	49	50	106	116
Ele. (degree)	35	22	42	82	55
IA (degree)	130 (-50)	107 (-73)	62	96 (-84)	90

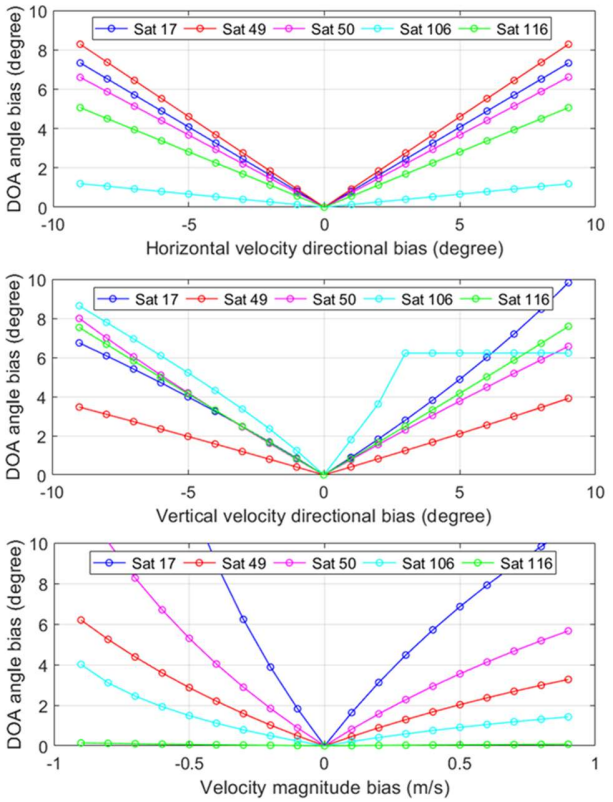

Fig. 10. The distribution of DOA estimation error (angle bias) for different velocity biases.

To illustrate the effect of velocity bias on DOA estimation, we apply three types of velocity offsets to healthy satellite observations: (1) horizontal directional bias (yaw error) in a range of ±10 degrees, (2) vertical directional bias (pitch error) in a range of ±10 degrees, and (3) magnitude bias in a range of ±1 meters/second. Table II lists the healthy satellites selected for the evaluation. Fig. 10 depicts how the estimated DOAs vary with different velocity biases. The results show that DOA angle bias increases as the velocity bias becomes larger. Under horizontal directional bias, satellites with higher elevation angles are less affected by DOA estimation. Since the satellite elevation is always above 0 degrees, the DOA estimation error remains smaller than the given horizontal velocity bias. As an example, when the horizontal velocity bias is 9 degrees, satellite 106 has a DOA angle bias of 1.2 degrees, while satellite 49 shows a bias of 8.2 degrees.

The DOA angle bias shows a similar increasing trend under vertical directional velocity bias, as observed with horizontal bias.

TABLE III
VELOCITY ESTIMATION RESULTS (MAG. MEAN: MEAN VELOCITY MAGNITUDE BIAS, MAG. MAX: MAXIMUM OF VELOCITY MAGNITUDE BIAS, ANG. MEAN: MEAN VELOCITY DIRECTIONAL BIAS, ANG. MAX: MAXIMUM OF VELOCITY DIRECTIONAL BIAS)

Mag. MEAN (m/s)	Mag. MAX (m/s)	Ang. MEAN (degree)	Ang. MAX (degree)
0.10	0.31	2.45	8.82

However, satellites with larger elevation angles experience greater DOA angle bias. Notably, satellite 116 has an included angle (IA) of 90 degrees between the receiver's velocity vector and the LOS vector. It shows a symmetric DOA bias trend as the vertical velocity bias varies from -9 degrees to 9 degrees. In contrast, other satellites exhibit asymmetric variations in DOA bias. For satellites with IA less than 90 degrees, the DOA bias increases more rapidly under negative pitch error. The opposite trend is observed for satellites with IA greater than 90 degrees. These results indicate that the DOA bias caused by vertical velocity error is influenced by both the satellite's elevation angle and its IA relative to the receiver's velocity vector.

The variation in DOA angle bias due to velocity magnitude bias is exclusively dependent on the IA between the DOA and the velocity direction. More specifically, it is specifically influenced by the degree of collinearity between them. Satellite 17, which has the smallest IA between the DOA and the velocity vector, shows the largest DOA angle bias under magnitude bias. In contrast, satellite 116, with a 90 degrees IA, is virtually unaffected. For all selected satellites, DOA bias is greater when the velocity magnitude is underestimated than when it is overestimated. This finding highlights the asymmetric impact of velocity magnitude bias on DOA estimation.

Overall, deviations in both the direction and magnitude of velocity affect the accuracy of the proposed DOA estimation. The extent of this effect depends on the deviation type, the satellite elevation, and the IA between DOA and velocity. Consequently, the proposed DOA estimation method requires an accurate velocity to ensure reliable performance.

C. NLOS Correction Evaluation in Urban Canyon 1

This section evaluates the NLOS correction performance of the proposed method. We first assess the velocity initialization using GLIO. Fig. 11 illustrates the magnitude and directional biases in velocity initialization. The driving period is indicated by green boxes. The results demonstrate high accuracy in velocity estimation during driving period. In contrast, a larger angle bias is observed during the parking period, likely due to drift of local position. Table III summarizes the detailed statistics.

To evaluate the effectiveness of NLOS correction, we compare the raw GNSS observations, the conventional 3DMA GNSS correction method [20, 33], and our proposed 3DLA NLOS correction method based on observation errors. Ground truth positions are used to calculate the raw observation errors and to initialize the 3DMA method. Fig. 12 compares the CDF of DD

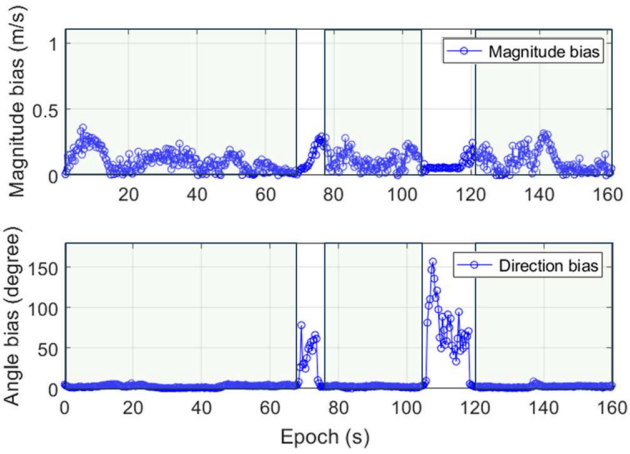

Fig. 11. The illustration of velocity initialization bias with GLIO. The upper part shows the magnitude bias while the direction bias is depicted at the bottom. Green boxes denote the driving period.

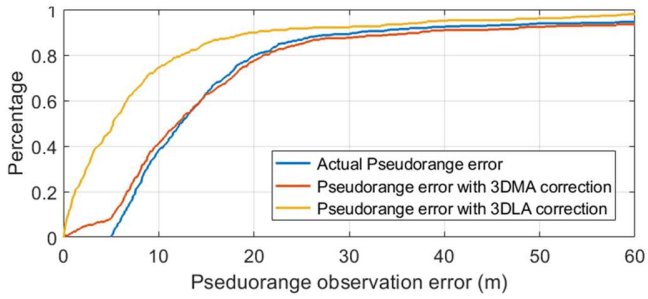

Fig. 12. The CDF of the actual observation error (double-difference pseudorange error labeled by ground truth position) and observation error after NLOS correction, including 3DMA-based and the proposed 3DLA-based methods. The actual observation error is depicted by dark blue, the corrected CDF of 3DMA and the proposed 3DLA method are given as red and orange curves, respectively.

pseudorange error before and after correction using 3DMA and the proposed 3DLA methods. The results show that approximately 20% of observations have errors exceeding 20 meters. Beyond the display area, the maximum error reaches up to 100 meters, likely due to long-range or multi-reflection NLOS receptions. The conventional 3DMA method provides limited improvement and fails to correct large NLOS errors. In contrast, the proposed method achieves more effective NLOS correction. The percentage of observations with errors exceeding 20 meters is reduced from 20.8% to 9.6%.

Fig. 13 provides a detailed comparison of actual and predicted pseudorange errors for individual NLOS receptions across epochs, using both 3DMA and 3DLA methods. The horizontal axis indicates the epoch index for each satellite, while the vertical axis shows the observation error in meters. For each epoch, three bars are shown: the actual observation error (purple), the 3DLA-predicted error (red), and the 3DMA-predicted error (orange). A close alignment between the predicted error and the actual error can be regarded as a successful correction. Table IV summarizes the NLOS correction performance, with mean correction error computed as the average difference between predicted and

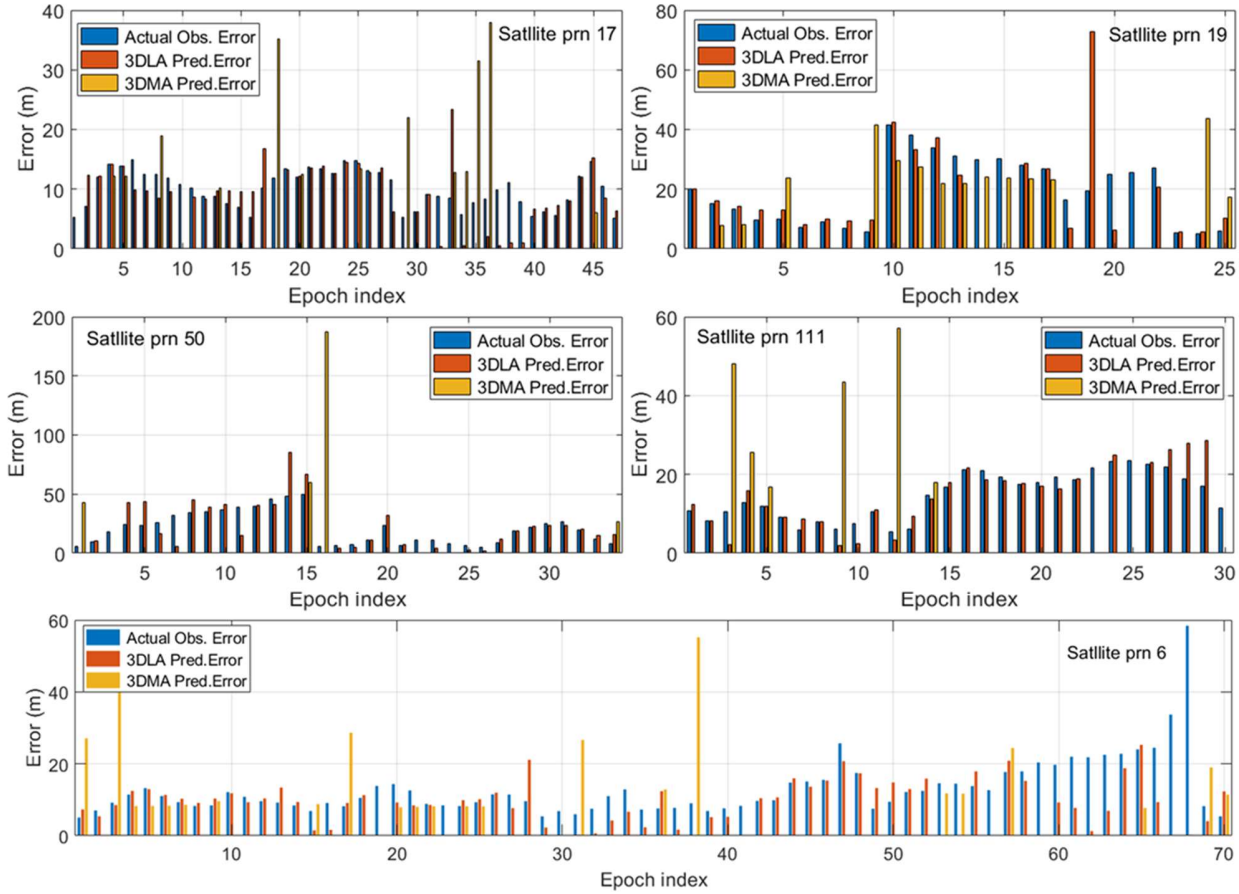

Fig. 13. Individual demonstration of the observation error and correction of selected satellites in Urban Canyon 1. The actual observation error (Actual Obs. Error) and the predicted error for correction among epochs by 3DMA (3DMA Pred. Error) and the proposed 3DLA (3DLA Pred. Error) methods are presented.

actual errors. The 3DMA method shows lower correction availability compared with the proposed approach. This is primarily due to the limitations of 3D city models. Their limited resolution and reconstruction accuracy hinder the reliable identification of reflection points on building facades.

For the available 3DMA results, significant discrepancies between predicted and actual errors suggest that NLOS paths are not correctly restored. For example, 3DMA underestimates the error for satellite 19 in most epochs. This discrepancy is caused by both the limited accuracy of the models and the shortest-path assumption used in 3DMA, which tends to select incorrect but shorter paths. In contrast, the proposed 3DLA method achieves significantly more reliable performance. As shown in Table IV, 3DLA method achieves high correction availability and strong consistency between predicted and actual observation errors across many epochs. For satellite 17, 3DMA achieves 27.7% correction availability, with a mean error of 9.8 meters and a standard deviation of 10.1 meters. In comparison, the 3DLA method achieves 95.7% availability, with a mean error of 2.9 meters and a standard deviation of 3.4 meters.

To better visualize and analyze the NLOS correction results, Fig. 14 illustrates the restored signal paths of selected satellites within the 3D PCM. At epoch 10, Satellite 19 is identified as NLOS with an observation error of 41.6 meters and an elevation angle of 39.5 degrees. The proposed 3DLA method successfully corrects this error, reducing it to 0.8 meters. The reflection path predicted by the 3DLA method is depicted in Fig. 14(a). The white line represents the blocked LOS path (denoted as the LOS signal), while the green and blue lines indicate the estimated DOA

ABLE IV
OVERVIEW OF THE NLOS CORRECTION RESULT FOR SELECTED SATELLITES (PRN: PSEUDORANDOM NOISE CODE, ELE.: ELEVATION ANGLE OF THE SATELLITE, MCE: MEAN CORRECTION ERROR, STD.: STANDARD DEVIATION OF MCE. AVAIL.: AVAILABILITY OF THE NLOS CORRECTION RESULT. 3DLA. AND 3DMA.: CORRECTION RESULT BY THE 3DMA METHOD AND 3DLA METHOD, RESPECTIVELY)

PRN		**6**	**17**	**19**	**50**	**111**
Ele. (degree)		47	49	39	23	43
3DMA	**MCE (m)**	9.0	9.8	12.4	61.9	24.6
	STD (m)	11.9	10.1	11.0	80.7	20.2
	Avail.	32.9%	27.7%	56.0%	11.8%	20.0%
3DLA	**MCE (m)**	**4.9**	**2.9**	**5.7**	**7.9**	**2.8**
	STD (m)	**8.0**	**3.4**	**11.4**	**8.9**	**3.3**
	Avail.	**88.6%**	**95.7%**	**88.0%**	**97.1%**	**93.3%**

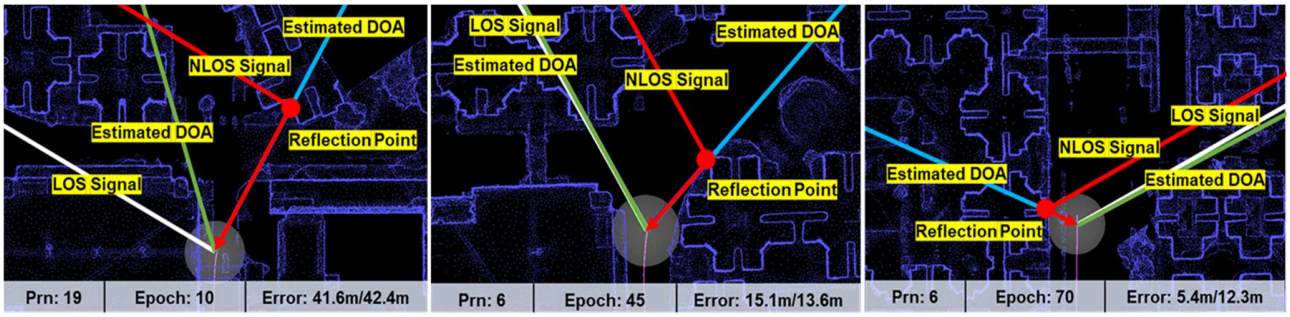

Fig. 14. The demonstration of the reflection restoration by the proposed method with the 3D PCM in Urban Canyon 1 in top view. The white line denotes the LOS path, the green and blue lines are predicted signal DOA by the proposed method. The red line represents the predicted signal transmission path by the proposed method. The error compares the actual observation error with predicted error by the proposed method.

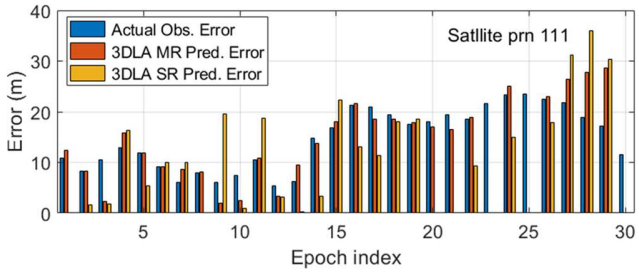

Fig. 15. Demonstration of the observation error and correction of satellite 111 with and without the multi-ray tracking strategy.

directions. Based on the DOA directions, the reflection point (red dot) and reflection path (red line, denoted as the NLOS signal) are reconstructed. The figure clearly shows that the LOS transmission path is obstructed by a building. Both estimated DOAs form large angles with the LOS direction. This suggests that the building facade is not parallel to the receiver's velocity direction, which is proved by the PCM data. Fig. 14(b) shows another correction for satellite 6 with an elevation angle of 47 degree. In this case, the building facade is approximately parallel to the driving direction, and the LOS is collinear to one of the estimated DOAs.

Fig. 13 also shows cases where the predicted observation errors from the proposed method deviate from the actual values. Most of the unsuccessful correction cases are caused by multipath reception. Notably, Doppler observations are only reliable in specific multipath scenarios, such as when there is one direct and one reflected signal, and the vehicle is moving parallel to the building facades [26]. In other cases, Doppler observations are greatly biased and DOA estimation is no longer valid. An example is shown in Fig. 14(c), where satellite 6 receives both a direct and a reflected signal while the vehicle is driving along the street. Since the vehicle velocity is parallel to the building facade, the red and green lines in the figure appear nearly collinear, with only a 1.2 degrees difference between the LOS and the estimated DOA. The predicted error for the reflected signal is 12.3 meters, whereas the actual observation error is 5.3 meters. This suggests that, when the moving direction of the receiver is parallel to the street, although we cannot accurately predict the observation error, the signal transmission paths of a multipath reception involving a direct and a reflected signal can still be reliably restored using the proposed method, .

Evaluation for Multi-ray Searching

This section presents the experimental evaluation of the proposed multi-ray search strategy for reflection point determination. Using satellite 111 as an example, Fig. 15 compares the NLOS correction results of the proposed method with multi-ray tracking (3DLA MR) and single-ray tracking (3DLA SR). Compared to 3DLA MR, the 3DLA SR method shows lower availability and greater inconsistency between predicted and actual observation errors. For example, in epochs 1, 8, 20, and 21, 3DLA SR fails to provide valid correction results. In epochs 2, 5, 9, 11, 14, 16, 17, 22, and 24, the predicted errors by 3DLA SR deviate more significantly from the actual errors. These issues arise from dynamic object artifacts, improper handling of signal penetration, model inaccuracies, and DOA estimation bias. On the one hand, single-line searching may fail to identify the correct reflection point due to artifacts or signal penetration, resulting in unavailable NLOS correction. On the other hand, for irregular building facades, even slight DOA bias or model inaccuracies may lead to incorrect reflection point generation and errors in NLOS correction. The proposed multi-ray searching strategy leverages local environmental similarity to generate multiple candidate reflection points and applies residual checks to identify the most probable one for NLOS correction. As demonstrated in Fig. 15, the 3DLA MR method outperforms 3DLA SR, achieving higher correction availability and improved accuracy.

D. NLOS Correction Evaluation in Urban Canyon 2

We further evaluate the NLOS correction performance of the proposed method in Urban Canyon 2 (Fig. 7), an area characterized by narrow streets and tall buildings. Fig. 16 and Table V provide the accuracy of velocity initialization and its variation over time during the experiment. High velocity estimation accuracy is maintained during the driving period. Fig. 17 compares the CDF of actual and predicted observation error using the 3DMA and proposed 3DLA methods. The 3DMA method is initialized using the ground truth position. The results show that about 66% of the NLOS observations have errors exceeding 20 meters. In this scenario, the conventional 3DMA method produces limited

TABLE V
VELOCITY ESTIMATION RESULTS (MAG. MEAN: MEAN VELOCITY MAGNITUDE BIAS, MAG. MAX: MAXIMUM OF VELOCITY MAGNITUDE BIAS, ANG. MEAN: MEAN VELOCITY DIRECTIONAL BIAS, ANG. MAX: MAXIMUM OF VELOCITY DIRECTIONAL BIAS)

Mag. MEAN (m/s)	Mag. MAX (m/s)	Ang. MEAN (degree)	Ang. MAX (degree)
0.16	0.44	3.54	7.02

TABLE VI
OVERVIEW OF THE NLOS CORRECTION RESULT FOR SELECTED SATELLITES (PRN: PSEUDORANDOM NOISE CODE, ELE.: ELEVATION ANGLE OF THE SATELLITE, MCE: MEAN CORRECTION ERROR, STD.: STANDARD DEVIATION OF MCE. AVAIL.: AVAILABILITY OF THE NLOS CORRECTION RESULT. 3DLA. AND 3DMA.: CORRECTION RESULT BY THE 3DMA METHOD AND 3DLA METHOD, RESPECTIVELY)

PRN		1	4	9	57	95	116
Ele. (degree)		42	20	28	41	49	51
3DMA	MCE (m)	15.8	110.3	50.6	22.9	38.5	39.0
	STD (m)	10.8	49.4	33.1	12.1	24.9	23.9
	Avail.	50.0%	4.3%	16.6%	18.8%	38.4%	20.0%
3DLA	MCE (m)	**7.4**	**74.5**	**23.8**	**9.2**	**21.5**	**20.5**
	STD (m)	**6.6**	**52.0**	**26.6**	**6.1**	**19.5**	**20.2**
	Avail.	**92.8%**	**86.9%**	**94.4%**	**100.0%**	**92.3%**	**93.3%**

correction performance. In contrast, the proposed 3DLA method significantly improves correction performance, reducing the proportion of large-error observations (over 20 meters) from 66% to 30%.

Fig. 18 compares the predicted observation errors of the 3DMA and 3DLA methods with the actual errors for selected satellites. Table VI provides the corresponding statistical summary. The results show a notable drop in correction availability for the conventional 3DMA method in Urban Canyon 2 compared to Urban Canyon 1. Furthermore, the 3DMA method demonstrates low correction accuracy. In contrast, the proposed 3DLA NLOS correction method achieves consistently higher availability and accuracy. For example, satellite 9 (epochs 2, 3, 4, 9, and 14), and satellite 116 (epochs 3 and 10). Fig. 19 provides a visualization of these correction results. However, many NLOS receptions with large errors remain uncorrected. One such case is satellite 4, which experiences severe NLOS receptions, with errors reaching up to 180 meters. In most epochs, the proposed method is unable to identify reflection paths that match the observed error. In these cases, the identified reflection points are still occluded by buildings along the signal path toward the satellite, suggesting the presence of multi-reflections. To explore possible multi-reflection paths, we trace the signal from the initial reflection point using a 3D building model and the law of reflection, as depicted in Fig. 19(d). The analysis reveals a triple reflection, with a predicted error exceeding

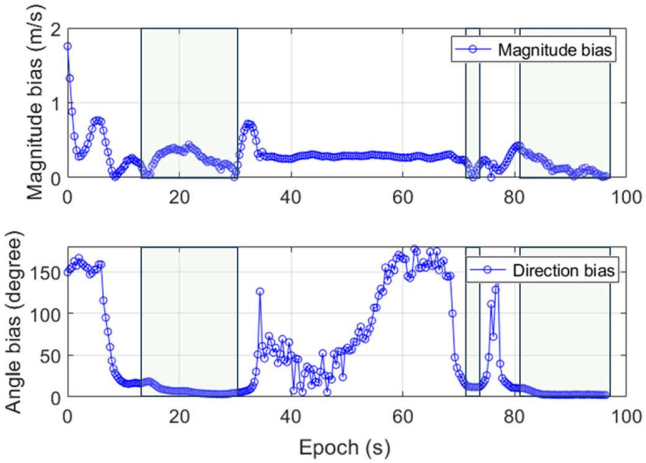

Fig. 16. The illustration of velocity initialization bias with GLIO. The upper part shows the magnitude bias while the direction bias is depicted at the bottom. Green boxes denote the driving period.

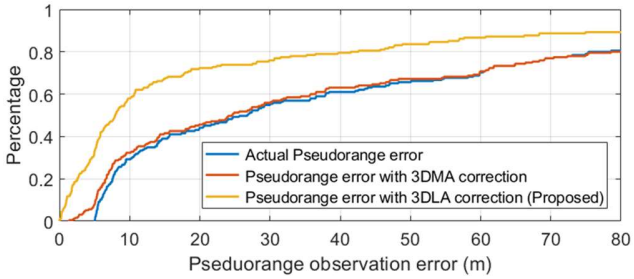

Fig. 17. The CDF of the actual observation error (double-difference pseudorange error labeled by ground truth position) and observation error after NLOS correction, including 3DMA-based and the proposed 3DLA-based methods. The actual observation error is depicted by dark blue, the corrected CDF of 3DMA and the proposed 3DLA method are given as red and orange curves, respectively.

160 meters, which closely matches the actual observed error. This further supports the effectiveness of proposed DOA estimation method.

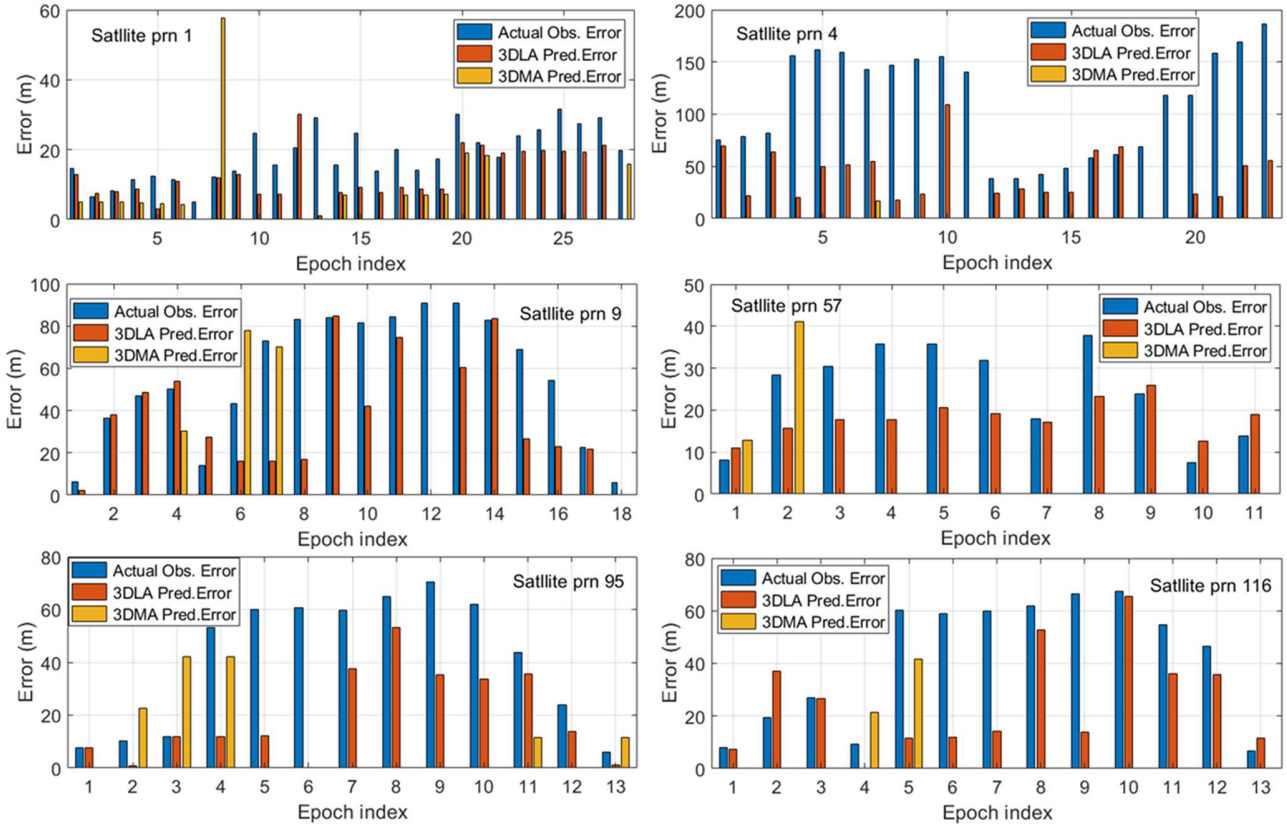

Fig. 18. Individual demonstration of the observation error and correction of selected satellites in Urban Canyon 2. The actual observation error (Actual Obs. Error) and the predicted error for correction among epochs by 3DMA (3DMA Pred. Error) and the proposed 3DLA (3DLA Pred. Error) methods are presented.

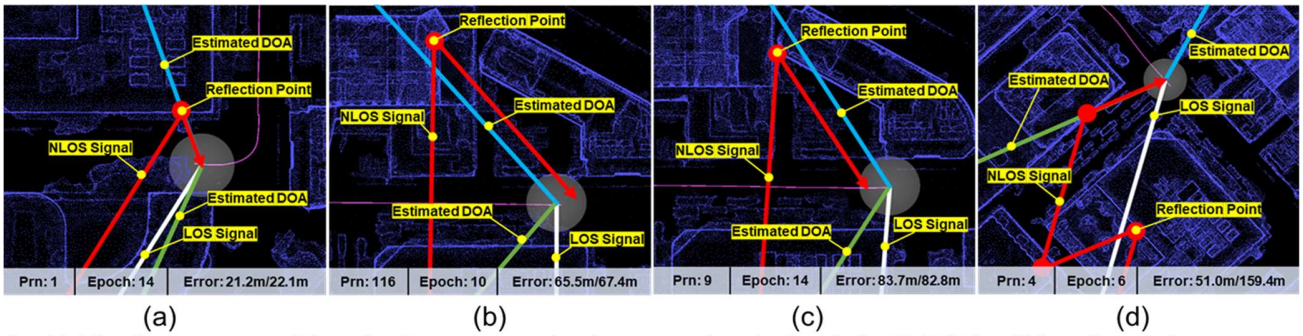

Fig. 19. The demonstration of the reflection restoration by the proposed method with the 3D PCM in Urban Canyon 2 in top view. The white line denotes the LOS path, the green and blue lines are predicted signal DOA by the proposed method. The red line represents the predicted signal transmission path by the proposed method. The error compares the actual observation error with predicted error by the proposed method.

E. Positioning Performance Evaluation Using the Proposed 3DLA NLOS Correction

To evaluate how the proposed NLOS correction improves positioning performance, we compare the following methods both qualitatively and quantitatively in Urban Canyon 1 and 2. The evaluation considers mean error, maximum error, and standard deviation in both 2D and 3D positioning. The evaluated methods are listed as follows:

(a) **LC-GNSS-LIO**: A loosely-coupled GNSS/LIO integration system (LIO-SAM) [34] fusing position-level GNSS solutions and LIO solutions. RTKLIB [35] is used to obtain differential GNSS solutions with filter type settings to "combined" and RAIM FDE enabled.

(b) **GLIO**: A tightly-coupled GNSS/LiDAR/INS integration system [27] using original GNSS raw measurements.

(c) **GLIO-COR**: GLIO with NLOS-corrected GNSS measurements, reflecting the impact of the proposed NLOS correction method.

The evaluation results are summarized in Table VII. All three methods are aligned by fixing the first epoch of the trajectory. Fig. 20 shows the 2D and 3D trajectories and positioning errors in Urban Canyon 1. For LC-GNSS-LIO, the 2D mean positioning error is 4.2 meters, with a maximum error of 6.6 meters and a standard deviation of 1.5 meters while the 3D positioning results

TABLE VII
POSITIONING PERFORMANCE OF THE EVALUATED METHODS IN URBAN CANYON 1 (2D MEAN AND 3D MEAN: 2D AND 3D POSITIONING ERRORS IN METERS. IMPR.: IMPROVEMENT CALCULATED BASED ON GLIO RESULTS. STD: STANDARD DEVIATION. MAX: MAXIMUM ERROR)

ALL DATA	URBAN CANYON 1			URBAN CANYON 2		
	LC-GNSS-LIO	GLIO	GLIO-COR	LC-GNSS-LIO	GLIO	GLIO-COR
2D MEAN (M)	4.2	2.8	**2.6**	9.0	**1.5**	1.6
2D MAX (m)	6.6	4.1	**3.9**	16.5	**4.3**	4.7
2D STD (m)	1.5	0.9	**0.7**	4.5	**0.7**	0.9
3D MEAN (m)	7.0	9.8	**4.3**	9.2	5.1	**3.2**
3D MAX (m)	12.5	15.9	**8.0**	17.0	8.2	**5.8**
3D STD (m)	3.8	3.9	**1.6**	4.7	2.1	**1.3**

show a mean error of 7.0 meters, a maximum error of 12.5 meters, and a standard deviation of 3.8 meters. At the start and end of the trajectory, the vehicle traverses through open intersections, where GNSS signal quality is significantly better, resulting in lower positioning errors. In contrast, the middle segment features a complex environment with degraded GNSS observations. As a result, even with FDE and forward-backward filtering, the loosely coupled system still suffers from large errors in this segment. Using raw GNSS measurements, GLIO achieves 2.8 meters horizontal accuracy with maximum error reaching 4 meters, which is greatly improved compared with the loosely coupled method. However, its 3D positioning accuracy degrades to 9.8 meters, with a maximum error of 15.9 meters. A noticeable Z-axis drift is observed in the GLIO trajectory due to severe NLOS receptions. With corrected GNSS measurements from the proposed method, GLIO-COR improves 2D positioning accuracy to 2.6 meters, and more importantly, the 3D positioning accuracy reaches 4.3 meters. The vertical drift is effectively reduced, which means that the proposed method effectively corrected a significant portion of the NLOS-contaminated observations.

Fig. 21 shows the 3D trajectories and positioning error curves of the three methods in Urban Canyon 2. Due to a further reduction in the availability of healthy GNSS observations, the standalone GNSS positioning solution experiences a significant decline in availability. Moreover, the available GNSS solutions exhibit consistently large positioning errors. As a result, the loosely coupled method yields significant trajectory errors. GLIO achieves a 2D mean error of 1.5 meters and a 3D mean error of 5.1 meters. The sharp turning points in both trajectories correspond to large observation errors during the parking period. After NLOS correction, the 3D positioning accuracy of GLIO-COR improves from 5.1 meters to 3.2 meters. However, its 2D positioning accuracy degrades, with the error increasing from 1.5 to 1.6 meters. After 60 seconds, the GLIO-COR trajectory exhibits an upward drift, likely due to dominant multipath and multi-reflection effects in the GNSS signals. These effects are not fully mitigated by the proposed correction approach.

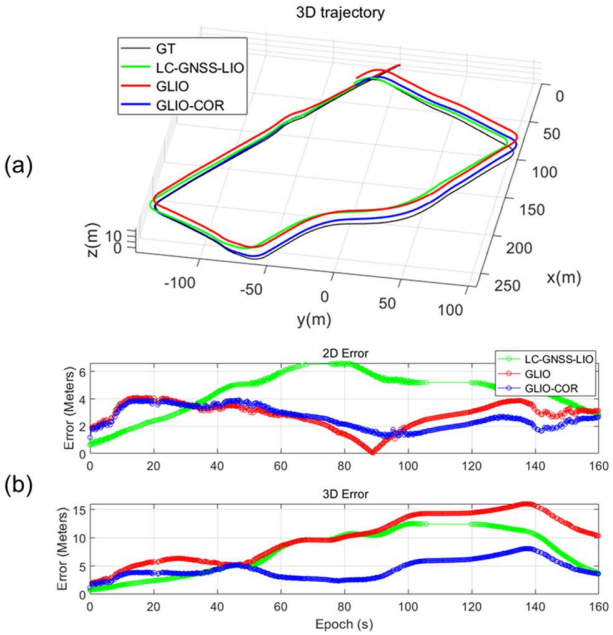

Fig. 20. The comparison of the trajectory and positioning error in Urban Canyon 1.

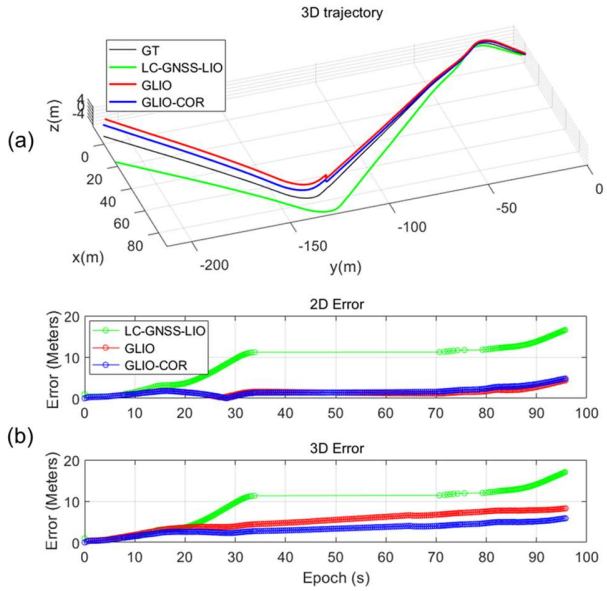

Fig. 21. The comparison of the trajectory and positioning error in Urban Canyon 2.

F. Running Efficiency Analysis

This section evaluates the processing time of the proposed method to demonstrate its computational efficiency for real-time applications. Experiments are conducted on a single-threaded i9-12900K CPU. The algorithm runtime is primarily composed of two components: DOA estimation and NLOS correction. In our evaluation, we set around 20 satellites for DOA estimation, requiring 0.8–1.1 ms per epoch. Such efficiency is attributed to the proposed optimization-based estimator. The NLOS correction includes multi-ray searching and reflection point determination, with the former being the most time-consuming. For satellites

where no reflection point is found, the computational cost is highest, since successful point detection enables early termination. Under the given experimental setup, the maximum multi-ray tracking time per satellite-in the absence of a reflection point-is approximately 12 ms. When a reflection point is found, the computation time ranges from 1 to 12 ms, with most cases under 5 ms. Since only a few satellites lack valid reflection points, the average processing time per satellite remains under 10 ms. Further efficiency improvements can be achieved by using smaller or sparser point clouds, which introduces a trade-off between computational cost and correction accuracy. Therefore, the proposed method achieves real-time performance and shows strong potential for practical ITS applications in challenging environments.

VI. Conclusion

GNSS positioning has long suffered from NLOS receptions in urbanized areas. Conventional NLOS correction methods use 3D models or 3D LiDAR to restore the signal transmission and correct NLOS error. However, their reliance on the shortest path assumption limits the accurate identification of true reflection path, let alone precisely correct NLOS observation. In this work, a 3D LiDAR-aided GNSS NLOS correction method is proposed, which: (1) develops a 3D LiDAR-aided GNSS DOA estimator using Doppler measurement, along with an analysis of how velocity bias affects estimation accuracy; (2) presents a NLOS correction method that integrates DOA estimation with PCM, leveraging multi-ray tracking and residual evaluation to robustly determine reflection points and enhance correction accuracy. The proposed method is evaluated on two challenging urban sequences in Hong Kong and demonstrates significantly more reliable NLOS correction performance than the conventional approach. Overall, the method achieves over 90% correction availability, with substantial improvements in NLOS observation accuracy. When integrated into a GNSS/LiDAR/INS framework, the proposed correction reduces 3D positioning errors from 9.8 to 4.3 meters in Urban Canyon 1, and from 5.1 to 3.7 meters in Urban Canyon 2. These results highlight the method's potential for improving urban positioning accuracy in complex environments.

Despite the improved positioning performance, residual errors remain at the meter level due to unmodeled multipath and multi-reflection effects. Future work may extend this framework by removing the single-reflection assumption. This can be achieved through PCM-based planar extraction combined with a shooting-and-bounce strategy to predict multi-reflection signal paths. In addition, the current residual-check strategy for selecting candidate corrections depends heavily on the quality of initial position estimates. Future research could explore consistency-based strategies for reflection path selection, reducing reliance on initialization accuracy.

References

[1] N. Alam and A. G. Dempster, "Cooperative positioning for vehicular networks: Facts and future," *IEEE transactions on intelligent transportation systems,* vol. 14, no. 4, pp. 1708-1717, 2013.

[2] E. D. Kaplan and C. Hegarty, *Understanding GPS/GNSS: principles and applications*. Artech house, 2017.

[3] J. K. Suhr, J. Jang, D. Min, and H. G. Jung, "Sensor fusion-based low-cost vehicle localization system for complex urban environments," *IEEE Transactions on Intelligent Transportation Systems,* vol. 18, no. 5, pp. 1078-1086, 2016.

[4] A. Fascista, G. Ciccarese, A. Coluccia, and G. Ricci, "Angle of arrival-based cooperative positioning for smart vehicles," *IEEE Transactions on Intelligent Transportation Systems,* vol. 19, no. 9, pp. 2880-2892, 2017.

[5] N. Zhu, J. Marais, D. Bétaille, and M. Berbineau, "GNSS position integrity in urban environments: A review of literature," *IEEE Transactions on Intelligent Transportation Systems,* vol. 19, no. 9, pp. 2762-2778, 2018.

[6] M. Petovello and P. Groves, "Multipath vs. NLOS signals," *Inside GNSS,* vol. 8, no. 6, pp. 40-42, 2013.

[7] M. S. Circiu *et al.*, "Evaluation of GPS L5 and Galileo E1 and E5a performance for future multifrequency and multiconstellation GBAS," *Navigation: Journal of The Institute of Navigation,* vol. 64, no. 1, pp. 149-163, 2017.

[8] J. Blanch, T. Walter, and P. Enge, "Fast multiple fault exclusion with a large number of measurements," in *Proceedings of the 2015 International Technical Meeting of the Institute of Navigation*, 2015, pp. 696-701.

[9] L.-T. Hsu, H. Tokura, N. Kubo, Y. Gu, and S. Kamijo, "Multiple faulty GNSS measurement exclusion based on consistency check in urban canyons," *IEEE Sensors Journal,* vol. 17, no. 6, pp. 1909-1917, 2017.

[10] L.-T. Hsu, Y. Gu, and S. Kamijo, "3D building model-based pedestrian positioning method using GPS/GLONASS/QZSS and its reliability calculation," *GPS solutions,* vol. 20, pp. 413-428, 2016.

[11] L. Lau and P. Cross, "Development and testing of a new ray-tracing approach to GNSS carrier-phase multipath modelling," *Journal of Geodesy,* vol. 81, pp. 713-732, 2007.

[12] W. Wen, G. Zhang, and L. T. Hsu, "Correcting NLOS by 3D LiDAR and building height to improve GNSS single point positioning," *Navigation,* vol. 66, no. 4, pp. 705-718, 2019.

[13] W. W. Wen and L.-T. Hsu, "3D LiDAR aided GNSS NLOS mitigation in urban canyons," *IEEE Transactions on Intelligent Transportation Systems,* vol. 23, no. 10, pp. 18224-18236, 2022.

[14] T. Suzuki and N. Kubo, "N-LOS GNSS signal detection using fish-eye camera for vehicle navigation in urban environments," in *Proceedings of the 27th International Technical Meeting of The Satellite Division of the Institute of Navigation (ION GNSS+ 2014)*, 2014, pp. 1897-1906.

[15] W. Wen, X. Bai, Y. C. Kan, and L.-T. Hsu, "Tightly coupled GNSS/INS integration via factor graph and aided by fish-eye camera," *IEEE Transactions on Vehicular Technology,* vol. 68, no. 11, pp. 10651-10662, 2019.

[16] W. W. Wen, G. Zhang, and L.-T. Hsu, "GNSS NLOS exclusion based on dynamic object detection using LiDAR point cloud," *IEEE transactions on intelligent transportation systems,* vol. 22, no. 2, pp. 853-862, 2019.

[17] W. Wen, "3D LiDAR aided GNSS and its tightly coupled integration with INS via factor graph optimization," in *Proceedings of the 33rd International Technical Meeting of the Satellite Division of The Institute of Navigation (ION GNSS+ 2020)*, 2020, pp. 1649-1672.

[18] S. Miura, L.-T. Hsu, F. Chen, and S. Kamijo, "GPS error correction with pseudorange evaluation using three-dimensional maps," *IEEE Transactions on Intelligent Transportation Systems,* vol. 16, no. 6, pp. 3104-3115, 2015.

[19] L.-T. Hsu, Y. Gu, and S. Kamijo, "NLOS correction/exclusion for GNSS measurement using RAIM and city building models," *Sensors,* vol. 15, no. 7, pp. 17329-17349, 2015.

[20] G. Zhang, H.-F. Ng, W. Wen, and L.-T. Hsu, "3D mapping database aided GNSS based collaborative positioning using factor graph optimization," *IEEE Transactions on Intelligent Transportation Systems,* vol. 22, no. 10, pp. 6175-6187, 2020.

[21] W. Wen, G. Zhang, and L.-T. Hsu, "Correcting GNSS NLOS by 3D LiDAR and building height," in *Proceedings of the 31st International Technical Meeting of the Satellite Division of The Institute of Navigation (ION GNSS+ 2018)*, 2018, pp. 3156-3168.

[22] X. Bai, W. Wen, and L. T. Hsu, "Using Sky-pointing fish-eye camera and LiDAR to aid GNSS single-point positioning in urban canyons," *IET Intelligent Transport Systems,* vol. 14, no. 8, pp. 908-914, 2020.

[23] M. G. Amin, X. Wang, Y. D. Zhang, F. Ahmad, and E. Aboutanios, "Sparse arrays and sampling for interference mitigation and DOA estimation in GNSS," *Proceedings of the IEEE,* vol. 104, no. 6, pp. 1302-1317, 2016.

[24] A. Vu, A. Ramanandan, A. Chen, J. A. Farrell, and M. Barth, "Real-time computer vision/DGPS-aided inertial navigation system for lane-level vehicle navigation," *IEEE Transactions on Intelligent Transportation Systems,* vol. 13, no. 2, pp. 899-913, 2012.
[25] L. Zhang, H.-F. Ng, G. Zhang, and L.-T. Hsu, "Ray-Tracing Correction for GNSS Velocity Estimation Using Doppler Frequency: A Feasibility Analysis," *IEEE Transactions on Instrumentation and Measurement,* 2024.
[26] P. Xie and M. G. Petovello, "Measuring GNSS multipath distributions in urban canyon environments," *IEEE Transactions on Instrumentation and Measurement,* vol. 64, no. 2, pp. 366-377, 2014.
[27] X. Liu, W. Wen, and L.-T. Hsu, "Glio: Tightly-coupled gnss/lidar/imu integration for continuous and drift-free state estimation of intelligent vehicles in urban areas," *IEEE Transactions on Intelligent Vehicles,* 2023.
[28] P. K. Enge, "The global positioning system: Signals, measurements, and performance," *International Journal of Wireless Information Networks,* vol. 1, no. 2, pp. 83-105, 1994.
[29] L.-T. Hsu *et al.*, "UrbanNav: An open-sourced multisensory dataset for benchmarking positioning algorithms designed for urban areas," in *Proceedings of the 34th International Technical Meeting of the Satellite Division of The Institute of Navigation (ION GNSS+ 2021)*, 2021, pp. 226-256.
[30] M. Quigley *et al.*, "ROS: an open-source Robot Operating System," in *ICRA workshop on open source software*, 2009, vol. 3, no. 3.2: Kobe, Japan, p. 5.
[31] S. Agarwal, K. Mierle, and T. C. S. Team, "Ceres Solver," 2023. [Online]. Available: https://github.com/ceres-solver/ceres-solver
[32] H. K. L. Department. "Hong Kong 3D Digital Map." https://3d.map.gov.hk/ (accessed.
[33] G. Zhang and L. T. Hsu, "Performance assessment of GNSS diffraction models in urban areas," *Navigation,* vol. 68, no. 2, pp. 369-389, 2021.
[34] T. Shan, B. Englot, D. Meyers, W. Wang, C. Ratti, and D. Rus, "Lio-sam: Tightly-coupled lidar inertial odometry via smoothing and mapping," in *2020 IEEE/RSJ international conference on intelligent robots and systems (IROS)*, 2020: IEEE, pp. 5135-5142.
[35] T. Takasu and A. Yasuda, "Development of the low-cost RTK-GPS receiver with an open source program package RTKLIB," in *International symposium on GPS/GNSS*, 2009, vol. 1: International Convention Center Jeju Korea Seogwipo-si, Korea, pp. 1-6.

Xikun Liu received his bachelor's degree in Mechanical Design, Manufacturing, and Automation from Huazhong University of Science and Technology, China in 2017, and master's degree in Mechatronics and Information Technology from Karlsruhe Institute of Technology, Germany in 2021. He is currently a Ph.D. candidate in the Department of Aeronautical and Aviation Engineering, the Hong Kong Polytechnic University. His research interests include GNSS and sensor-aided GNSS positioning, SLAM, and multiple sensor fusion in autonomous driving.

Weisong Wen (Member, IEEE) received a BEng degree in Mechanical Engineering from Beijing Information Science and Technology University (BISTU), Beijing, China, in 2015, and an MEng degree in Mechanical Engineering from the China Agricultural University, in 2017. After that, he received a PhD degree in Mechanical Engineering from The Hong Kong Polytechnic University (PolyU), in 2020. He was also a visiting PhD student with the Faculty of Engineering, University of California, Berkeley (UC Berkeley) in 2018. Before joining PolyU as an Assistant Professor in 2023, he was a Research Assistant Professor at AAE of PolyU since 2021. He has published 30 SCI papers and 40 conference papers in the field of GNSS (ION GNSS+) and navigation for Robotic systems (IEEE ICRA, IEEE ITSC), such as autonomous driving vehicles. He won the innovation award from TechConnect 2021, the Best Presentation Award from the Institute of Navigation (ION) in 2020, and the First Prize in Hong Kong Section in Qianhai-Guangdong-Macao Youth Innovation and Entrepreneurship Competition in 2019 based on his research achievements in 3D LiDAR aided GNSS positioning for robotics navigation in urban canyons. The developed 3D LiDAR-aided GNSS positioning method has been reported by top magazines such as Inside GNSS and has attracted industry recognition with remarkable knowledge transfer.

Liyuan Zhang received his B.E. degree in electronic and information engineering from the Chongqing University of Posts and Telecommunications, China. He received his M.S. degree in electronic and communication engineering from Beihang University, China. He is currently a PhD candidate in the Department of Aeronautical and Aviation Engineering, The Hong Kong Polytechnic University. His research interests include 3D mapping-aided GNSS velocity estimation in urban canyons.

Li-Ta Hsu received B.S. and Ph.D. degrees in aeronautics and astronautics from National Cheng Kung University, Taiwan, in 2007 and 2013, respectively. He is currently an associate professor with the Department of Aeronautical and Aviation Engineering. The Hong Kong Polytechnic University, before he served as a post-doctoral researcher at the Institute of Industrial Science at the University of Tokyo, Japan. In 2012, he was a visiting scholar at University College London, the U.K. His research interests include GNSS positioning in challenging environments and localization for pedestrians, autonomous driving vehicle, and unmanned aerial vehicle.